Experiments in Fluids [Suppl.] S78–S84 © Springer-Verlag 2000

# Defocusing digital particle image velocimetry: a 3-component 3-dimensional DPIV measurement technique. Application to bubbly flows

**F. Pereira, M. Gharib, D. Dabiri, D. Modarress**



**Abstract** This paper describes a three-dimensional imaging system for the purpose of mapping two-phase bubbly flows. The defocusing digital particle image velocimetry instrument records high resolution images of the bubble field and is capable of providing bubble size and bubble location within a cubic foot volume. The velocity field is calculated from the volumetric cross-correlation of consecutive three-dimensional sets of bubble locations. The bubble size information is estimated from the bubble scattered peak intensity. Both quantities correlate following a power law, as predicted by the Mie scattering theory. The technique is applied to the study of the dynamics of sub-millimeter air bubbles in a three-dimensional vortical flow generated by a propeller. Velocity, bubble size distribution and void fraction are briefly discussed.

## 1 Introduction

Air bubbles are created in large quantities in the wake of ocean vessels by propeller cavitation, by surface entrainment through free surface wave breakage by the ship's bow and stern, or by air entrainment in the turbulent boundary layer near the hull. Because of their large acoustical cross sections, they are responsible for the acoustical signature of the wake, which is known to persist for long periods of time. Larger bubbles will rise to the surface within a very short period of time, resulting in a surface slick detectable by radar or by altitude imaging devices (Griffin et al. 1992). There has been considerable interest in determining the air bubble population, thus resulting in much progress, especially in the area of bubble acoustics (Trevorrow et al. 1994) and cavitation inception (Billet 1985). Nevertheless, the coupling between bubbles and turbulent flows is far from understood. The experimental approaches in free surface water tunnels and tow tanks can provide an insight into the field of bubbly flow dynamics. However, the turbulent, multi-phase and three-dimensional nature of the flow demands experimental capabilities beyond standard single point measurement techniques (Naqwi et al. 1991) or planar imaging systems (Grant et al. 1995). A non-intrusive diagnostic instrument is needed, capable of mapping the surrounding flow field and tracking the spatial and temporal history of bubbles, with sufficient sensitivity to accurately estimate the void fraction, in three dimensions and within a reasonably large volume. Existing three-dimensional techniques such as holography (Barnhart et al. 1994), neutron radiography (Mishima and Hibiki 1998), Doppler tomographic imaging (Chen et al. 1997), particle tracking (Stüer et al. 1999), multilayer particle imaging (Abe et al. 1998) or scanning particle imaging (Brücker 1997) suffer from extreme complexity, insufficient spatial or temporal resolution, and/or lack of capability to measure both size and velocity data.

In this paper, we present an intrinsically three-dimensional imaging system based on the defocusing concept introduced by Willert and Gharib (1992). This system is capable of real-time imaging of bubbly flows, providing both bubble size and velocity information in three dimensions. In the first part, we describe the defocusing concept and its practical implementation. In the second part, we present in detail the accuracy analysis performed to determine the instrument performance, followed by a specific study for the size measurement. Finally, we apply the technique to map a vortical flow generated by a propeller and seeded with sub-millimeter air bubbles.

F. Pereira (✉), M. Gharib, D. Dabiri, D. Modarress
Center for Quantitative Visualization
California Institute of Technology
Pasadena, CA 91125, USA

The visit of Dr. F. Pereira to the C.Q.V. was made possible by a fellowship of the Fundação para a Ciência e a Tecnologia, Portugal, under the supervision of Professor M. V. Heitor (Instituto Superior Técnico, Lisbon).

The research was supported by the Office of Naval Research (contract N00014-97-1-0303), under the direction of Dr. E. P. Rood and Dr. M. Hyman. The defocusing digital particle image velocimetry (DDPIV) technology is protected under a US pending patent filed by California Institute of Technology.

The authors would like to thank F. Taugwalder for his expertise in designing the real-time image acquisition system.

## 2 Defocusing digital particle image velocimetry

### 2.1 Principle

To fully describe the defocusing digital particle image velocimetry (DDPIV) technique, a simplified two-dimensional imaging system is represented in Fig. 1. In Fig. 1a, a small aperture within the lens shows a solid angle of light rays emanating from two point sources, A and B. Point A is located on the reference plane (or object plane), while point B is located at a distance from this plane. Point A appears focused in A′, while B is projected as a blurred

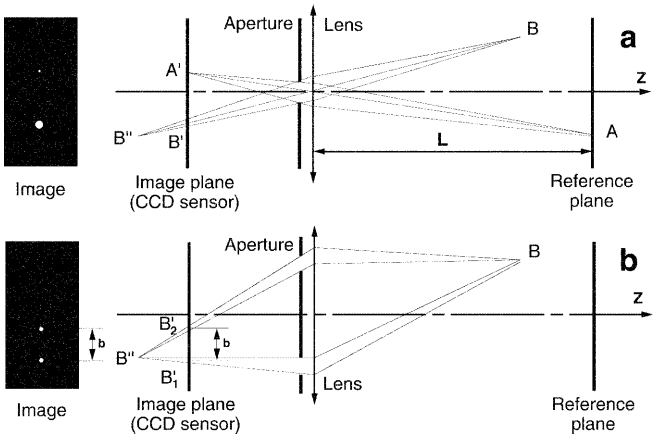


**Fig. 1a, b.** The defocusing principle: **a** standard imaging system; **b** defocusing arrangement

image B′. In this configuration, the depth location of the points is not recoverable. In the DDPIV technique, two or more apertures are shifted away from the centerline to obtain multiple images from each scattering source, as shown in Fig. 1b. The DDPIV technique uses the image shift $b$ caused by off-axis apertures for the measurement of the depth location of the source points, whereas the scattered light combined with the blurredness is used to recover the size information.

With a two-aperture mask, there exist two different locations, front and back of the reference plane, from which a particle forms exactly the same image pair. To overcome this non-uniqueness problem, we adopted a mask with three apertures forming an equilateral triangle, as shown in Fig. 2. The orientation of the triangle indicates the relative position of the source with respect to the reference plane.

## 2.2
## Determination of three-dimensional coordinates

Let $M$ be the geometrical magnification, $d$ the distance between the centers of the apertures and L the distance from the aperture plane to the reference plane. $M$ is equal to $h(L - a)/a(L + d)$, where $a$ is the characteristic size of the volume to be mapped, and $h$ is the height of the imaging sensor. The coordinates $(X,Y,Z)$ of $B$ in the camera coordinate system are derived from the image coordinates $(x'_1, y'_1)$ and $(x'_2, y'_2)$ of the projections $B'_1$ and $B'_2$ on the image plane (see Fig. 1b):

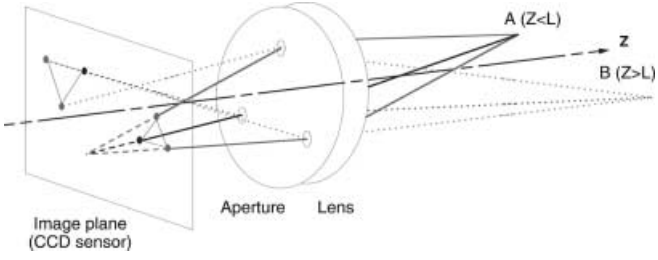


**Fig. 2.** Three-aperture defocusing arrangement

$$\begin{cases} X = \frac{b-2x'_1}{2\left(M+\frac{b}{d}\right)} = \frac{-b-2x'_2}{2\left(M+\frac{b}{d}\right)} \\ Y = -Kdy'_1Z = -Kdy'_2Z \\ Z = \frac{1}{\frac{1}{L}+Kb} \quad \text{with } K = \frac{1}{MdL} \end{cases} \tag{1}$$

where $b$ is the norm of the separation vector **b**:

$$b = \frac{Md}{Z}(L - Z) \tag{2}$$

These relations are shown to be equivalent to those of the defocusing concept originally introduced by Willert and Gharib (1992).



## 2.3
## Error analysis

We restrict our analysis, for sake of simplicity, to a two-dimensional configuration, where $Z$ is the main optical axis and $X$ is the in-plane axis. The particle image displacements $\mathrm{d}x'_1$ and $\mathrm{d}x'_2$ in the image plane are defined by:

$$\begin{aligned} \mathrm{d}x'_1 &= \frac{\partial x'_1}{\partial X}\mathrm{d}X + \frac{\partial x'_1}{\partial Z}\mathrm{d}Z = a_1\mathrm{d}X + b_1\mathrm{d}Z \\ \mathrm{d}x'_2 &= \frac{\partial x'_2}{\partial X}\mathrm{d}X + \frac{\partial x'_2}{\partial Z}\mathrm{d}Z = a_2\mathrm{d}X + b_2\mathrm{d}Z \end{aligned} \tag{3}$$

Solving Eq. (3) for the displacements $\mathrm{d}X$ and $\mathrm{d}Z$, we obtain the following relations:

$$\begin{aligned} \mathrm{d}X &= \frac{b_2\mathrm{d}x'_1 - b_1\mathrm{d}x'_2}{a_1b_2 - a_2b_1} \\ \mathrm{d}Z &= \frac{a_2\mathrm{d}x'_1 - a_1\mathrm{d}x'_2}{a_2b_1 - a_1b_2} \end{aligned} \tag{4}$$

Let us assume that the uncertainties in the geometrical parameters are neglectable and that the errors in the image plane $\mathrm{d}x'_1$ and $\mathrm{d}x'_2$ are equal such that:

$$\delta(\mathrm{d}x'_1) = \delta(\mathrm{d}x'_2) = \delta(\mathrm{d}x') \tag{5}$$

where $\delta$ represents the error in a given variable.

A measure of the overall system performance is given by the ratio between the out-of-plane and the in-plane errors, $\Delta Z$ and $\Delta X$, as commonly used with stereoscopic configurations. This quantity is referred to as the error ratio $e_\mathrm{r}$. One can show, using standard error analysis, that $e_\mathrm{r}$ is expressed by the quantity:

$$e_\mathrm{r} = \frac{\Delta Z}{\Delta X} = \frac{2Z}{\sqrt{4X^2 + \mathrm{d}^2}} \tag{6}$$

The resolution requirements are the following:

$$\begin{cases} \Delta X < \frac{k_X}{M}, \quad k_X = 0.01\,\text{pixel} = 10^{-4}\,\text{mm} \\ \Delta Z < k_Z a, \quad k_Z > 0 \end{cases} \tag{7}$$

Let $r_X = k_X/M$ and $r_Z = k_Z a$. We can write the following inequality defining the geometrical condition upon which the resolution requirements above are both verified:

$$\Delta Z < r_Z \Rightarrow d > 2\sqrt{\left(\frac{r_X}{r_Z}\right)^2 Z^2 - X^2} \tag{8}$$

Consider the worst case: $Z = L$ and $X = 0$ (centerline on the reference plane). We show that the distance $d$ between the apertures must satisfy the following inequality:

$$d > \frac{2L^2}{\frac{k_Z}{k_X} h(L-a) - 2L} \tag{9}$$

To observe a volume of one cubic foot ($a \approx 300$ mm ) and for $k_Z = 0.05\%$ of the full scale, one should take $L = 1265$ mm and $d = 76.4$ mm. The in-plane error is $\Delta X \approx 4.6$ μm and the corresponding error ratio $e_r = \Delta Z/\Delta X \approx 32$, thus $\Delta Z \approx 147.2$ μm for $X = 0$ and $Z = L$.



## 3 DDPIV system

### 3.1 Optical setup: camera and illumination

Because of the distance between the apertures, imposed by the resolution requirements, the three-aperture concept depicted in Fig. 2 is implemented using separated lenses. A charge coupled device (CCD) sensor is placed immediately behind each lens and radially moved from the lens optical axis. This design is shown to be strictly equivalent to the previous single lens design (Gharib et al. 1998). Moreover, it eliminates the problem of image overcrowding inherent in the original concept and allows one to observe higher density bubble/particle fields.

Three lens/aperture modules arranged in the shape of an equilateral triangle compose the optical system (see Fig. 3). An 8-bit digital 1k × 1k pixels CCD sensor is placed behind each module. Each sensor is positioned using a separate high precision three-translation and three-rotation stage. The triangle image of the scattering source is obtained by combining the three separated 8-bit images into a single 3 × 8-bit image suitable for processing.

Unlike planar PIV, the region of interest for DDPIV is a volume and therefore requires much more light intensity for illumination. Also, flows of relatively high velocities are to be observed, for which a pulsed light source is necessary. Moreover, a single wavelength with the least absorption is required for water applications. To satisfy these criteria, we use a frequency-doubled dual YaG laser delivering 125 mJ per pulse at 532 nm. The duration of a laser pulse is less than 10 ns. An optical arrangement expands and forms a cylindrical volume of collimated light with a diameter of 200 mm. The minimum measured $\Delta t$ for a DDPIV image pair is 400 ns.

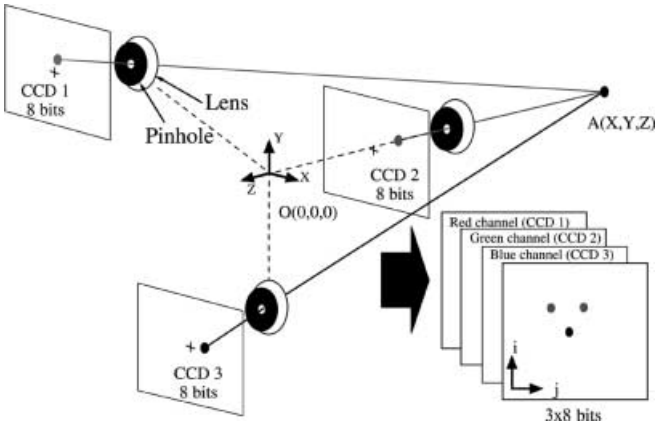


**Fig. 3.** The DDPIV camera schematic

### 3.2 Real-time acquisition and processing

The images from the DDPIV camera are recorded using a custom-made high-bandwidth data acquisition system. The images are acquired by three digital framegrabbers, each channel (1k × 1k, 8-bit data) being transferred to an 81-Gbyte disk at 30 frames per second and for a duration of up to 15 min.

The processing steps can be itemized as follows. First, for each plane of the 3 × 8-bit image, every bubble/particle gray-level image is fitted by a two-dimensional axisymmetric Gaussian curve. The standard deviation $\sigma$, the centroid and the amplitude of this Gaussian surface are optimized by a standard least-square minimization routine. Secondly, a search is done to identify triplets of fitted bubble/particle images that form an equilateral triangle. The size and centroid location of any completed triangle describes the $(X,Y,Z)$ coordinates through the relations in Eq. (1). In a third and final step, the displacement of each bubble is determined by a three-dimensional cross-correlation of voxels (volume elements) from two sequential DDPIV bubble data sets representing the bubble locations. The interrogation voxel is marched through the whole volume, in the physical cartesian space, as one would do in standard PIV using a pixel-based window. The computed displacement vectors are then divided by the laser pulse interval $\Delta t$ to produce a three-dimensional three-component velocity field. Finally, post-processing routines are used to re-interpolate and smooth the three-dimensional vector field in order to remove spurious vectors.

## 4 Error measurement

### 4.1 Position

A 12 in. × 12 in. glass plate is used, with a surface accuracy of 4–6 wavelengths/in. The paint covering one of the faces was removed to form a grid pattern of 625 round dots with a spacing of 12.7 mm and a nominal diameter of 1.5 ± 0.2 mm. The other face was ground to make it diffusive to light. The plate is imaged at 18 locations within the foot-cube interrogation volume, starting at the reference plane ($Z = -1265$ mm). The plate is moved along the $Z$-axis by increments of 10 mm by means of a motorized translation stage.

Figure 4 represents the in-plane and out-of-plane respective mean error and standard deviation, at each station along the $Z$-axis. The average errors on the $X$–$Y$ plane and on the $Z$ direction are found to be 42 μm and 658 μm, respectively. The in-plane error corresponds to 0.08 pixel, whereas the out-of-plane error represents about 1.3 pixels. These values are higher than those predicted by the error analysis presented earlier. This is explained by the fact that the optical concept used for this error analysis was for a

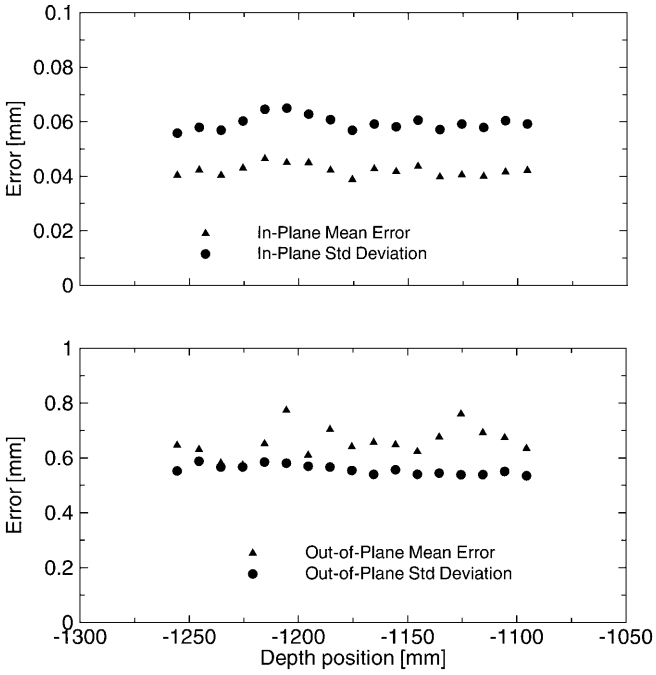


**Fig. 4.** In-plane (*top*) and out-of-plane (*bottom*) location errors

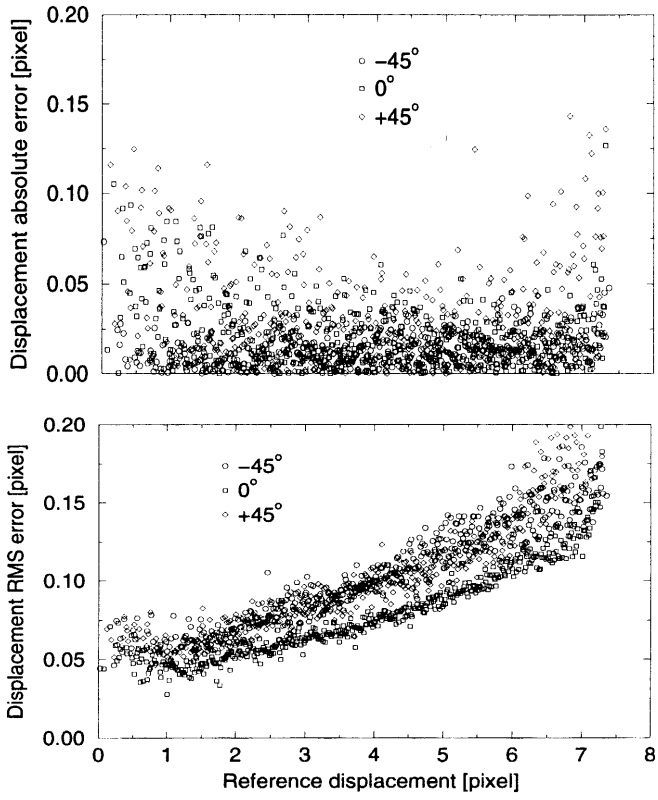


**Fig. 5.** Displacement absolute error (*top*) and rms error (*bottom*)

two-dimensional arrangement. Moreover, we did not take into account error sources such as the optical and geometrical distortions, which are not compensated here. The error ratio $e_r = \Delta Z/\Delta X$ is for this reason about twice as low as the theoretical value.

### 4.2 Velocity

The velocity error is established using a flat and rigid disk 300 mm in diameter, covered with a random pattern of approximately 7000 Gaussian dots with a standard deviation of 0.5 mm. The disk is put into rotation using a stepper motor, with its center placed at $Z = -1000$ mm and on the optical axis of the camera. The tangential velocity at the outer radius is set to 1 m/s $\pm$ $5 \times 10^{-4}$. Measurements are performed for three angular positions of the disk about the vertical $Y$-axis: +45°, 0° and −45°. For each position, a sequence of 64 image pairs is acquired. The time interval between images of a pair is 3.948 ms.

Errors are computed over 64 velocity vector fields, for each of the three angular positions considered, and comparison is done against the local true velocity. Figure 5 shows the absolute and the root mean square (rms) errors on the velocity measurements, converted into image displacements (pixel units). The absolute errors are constant over the range of displacements with an average value of 0.025 pixels. This value is higher, but yet acceptable, than the in-plane resolution requirement reported in the design stage [see Eq. (7)]. The rms errors are found to increase almost linearly with the displacement, though the errors at the limits of the measured range of displacements depart from this trend. This edge effect is caused by the truncated particle spatial distribution in these regions. Finally, the $Z$-component present in the non-zero angular positions causes the rms errors to be higher than those found at 0°. Indeed, the error on the out-of-plane component was shown to be 15 times higher than the error on the in-plane component (see Fig 4).

## 5 Size measurement methodology

The knowledge of the size distribution of air bubbles is a matter of great difficulty for which various techniques are available. A review of some of these methods is given by Billet (1985): nuclear (gamma ray, neutrons), electrical (Coulter counter), acoustical (attenuation, Doppler), optical (light scattering, photography, holography, phase detection). The light scattering techniques are the most widely used to determine bubble distributions. Katz et al. (1983) used a white light source for scattering. Different methods have also been developed based on laser Doppler techniques, the principle being that the measured maximum scattered intensity of a microbubble as it passes through a coherent laser light beam can be uniquely related to the size of the microbubble (see Billet 1986). Another interesting approach was by Rockwell et al. (1993), who used a scanning laser beam to interrogate the particle field of interest.

The Lorenz–Mie theory provides the exact solution to the problem of scattering of light by a single, homogeneous sphere of arbitrary size (Van de Hulst 1957). This theory relates the particle/bubble scattering intensity to the sphere size. Although the Mie solution is difficult to apply, it can be approached by geometrical optics. Using this method, Davis (1955) calculated the angular intensity distribution of the light scattered by an air bubble in water.

The intensity was found to increase rapidly for angles approaching the critical scattering angle of 82.8°. The scattered irradiance in this region was found to increase monotonically with bubble radius $a$, provided $a \gg \lambda$, where $\lambda$ is the wavelength of light in water (Dean and Marston 1991).

In this study, the size measurement procedure consists of measuring the intensity of the light scattered by calibrated glass microspheres. Seven diameters are considered: 99.6, 200, 278, 400, 480, 756 and 1008 μm. These particles have a known standard deviation: 3.5 μm for the smallest size and 37.1 μm for the largest sphere. A small number (4) of particles of each size category are placed on the adhesive side of a highly transparent and very thin tape stripe. This matrix is then immersed into a water tank and moved along the camera $Z$-axis by increments of 50 mm, between $Z = -1100$ and $Z = -400$ mm. A white light source is used to illuminate the matrix in a forward scatter mode with an angle of approximately 30°. The acquired images are processed through the DDPIV procedure described before. The mean peak amplitude of the two-dimensional Gaussian curves used to fit each of the three images of a particle is taken as the maximum scattered intensity of this particle, referred to as $I_a$. This intensity is therefore expressed in terms of gray levels, in the range 0–255, and is adjusted locally to correct for the spatial non-uniformity of the illumination. This is done by interpolating the intensity of particles with a given size placed at different locations across the particle matrix.

Figure 6 represents the peak intensity $I_a$ divided by 255, for all sphere sizes and all $Z$ stations. Intensity fluctuations are visible along the $Z$-axis and follow a similar trend for every size. Such fluctuations are essentially due to the adjustments applied, during the measurement, to the CCD sensors gain and to the light source power. Indeed, adjustments were made necessary to avoid image saturation. To account for that, one needs to select a global reference intensity $I_0$: we choose arbitrarily the intensity measured for the sphere with radius $a = 240$ μm.

Let $I = I_a/255$. Figure 7 displays the normalized intensity $I/I_0$ averaged over all $Z$ positions vs. the sphere radius $a$. The error bars indicate the standard deviation on the measurement of the particle image peak intensity $I$ and

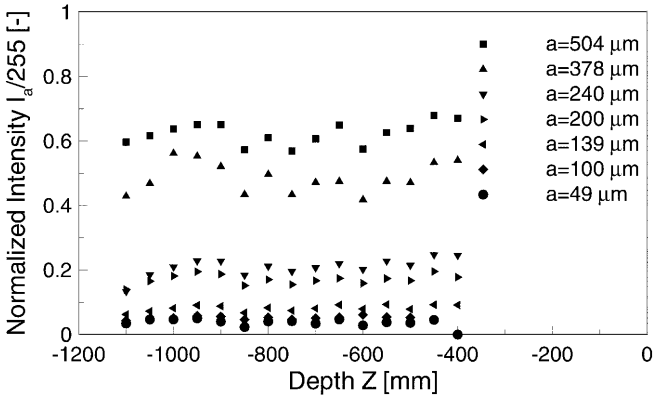


**Fig. 6.** Normalized peak intensity of particle image vs. depth Z for all values of the particle radius $a$

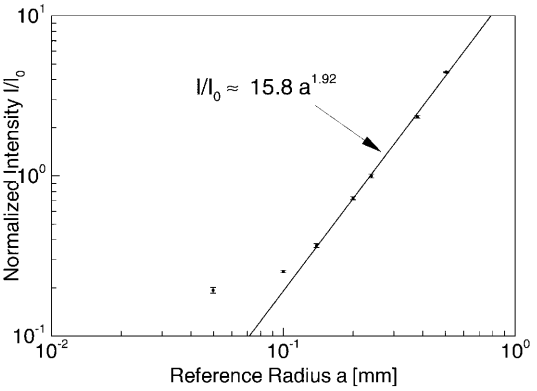


**Fig. 7.** Normalized scattered intensity vs. nominal radius $a$ and power fit

varies between 5.6% for $a = 504$ μm and 20% for $a = 49$ μm. The log–log representation shows a power law relationship. The power of the fitting curve (≈1.92 ) is found to correspond to the theoretical value of 2 derived from the Mie scattering theory (Van de Hulst 1957) and found experimentally by other researchers (Landa and Tebay 1970). This result suggests that one could use such a relation to make effective and accurate size measurements based on the particle/bubble intensity, provided a reference intensity is available at every location in the interrogation volume. An in-depth procedure, similar to that used by Hofeldt and Hanson (1991), should be performed to complete these preliminary results. Finally, as one would expect from the spatial accuracy measurements presented earlier, the spatial resolution of the current DDPIV system is here clearly bounded to radii no larger than 100 μm. This value corresponds to blurred bubble images with less than 4 pixels, inducing overestimated values for the width and amplitude of the two-dimensional Gaussian function used to fit the image. One can overcome this limit by using higher resolution image sensors.

## 6
## Application: propeller flow

In an attempt to demonstrate the functionality of the DDPIV imaging system, our final purpose consists of applying the technique to the observation and preliminary study of the dynamics of air bubbles injected into a three-dimensional vortical flow generated by a propeller. A two-blade model boat propeller with a diameter of 67 mm is immersed into a 1 $m^3$ water tank. The rotation speed is 12 rps and the tangential velocity is 2.52 m/s at the blade tips. A custom-made bubble generator is placed 500 mm below the propeller, producing a rising stream of sub-millimeter air bubbles. Phase averaging is performed on a sequence of 50 velocity vector fields.

### 6.1
### Velocity field

A three-dimensional velocity field is obtained after averaging and outlier correction. Massless particles are then numerically injected into the experimental mean velocity data set, in a radial arrangement and one diameter up-

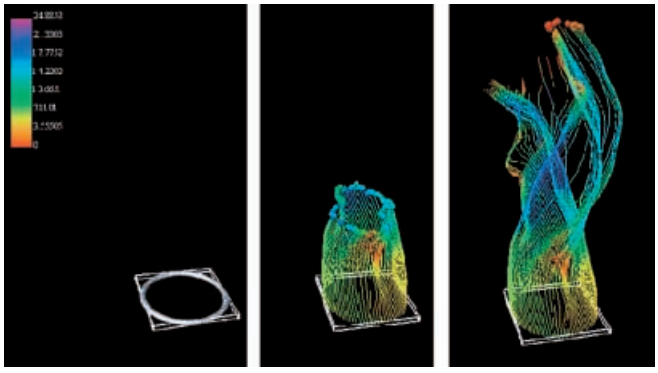

**Fig. 8.** Pathlines of bubbles around the propeller

stream of the propeller. The paths of the bubbles are determined (see Fig. 8). Color/gray level relates to the local measured velocity amplitude. Rising vertically in the upstream section of the flow, bubbles are trapped in the vortical flow induced by the propeller. Velocity reaches a maximum of 2.49 m/s in the outer region of the propeller, matching closely the blade tip tangential velocity.

### 6.2
### Size distribution

The mean radius along the $Y$ vertical axis of the flow (rotation axis of the propeller) is reported in Fig. 9. The mean radius increases almost linearly until $Y \approx 30$ mm, where the propeller is located. Then the radius follows the opposite trend, reaching back a value of approximately 200 μm. The growth of bubbles is, to a very small extent ($\ll 1\%$), due to the decrease in the static pressure with increasing $Y$. In fact, bubbles experience first the low pressure existing in the suction side of the propeller, before getting into the high pressure region where they collapse. In Fig. 10, we report the histograms considering the same volume below and above $Y = 30$ mm. The ratio of the upstream to the downstream populations is 65%. However, the ratio of the respective void fractions ($V_f$) is close to 100%. These observations indicate that coalescence of bubbles is the main mechanism acting here, although breakup may occur in the propeller region. Such conclusions are obviously limited to this specific flow: void fraction and population will vary in higher speed flows and/or in the presence of bubble generating mechanisms such as cavitation.

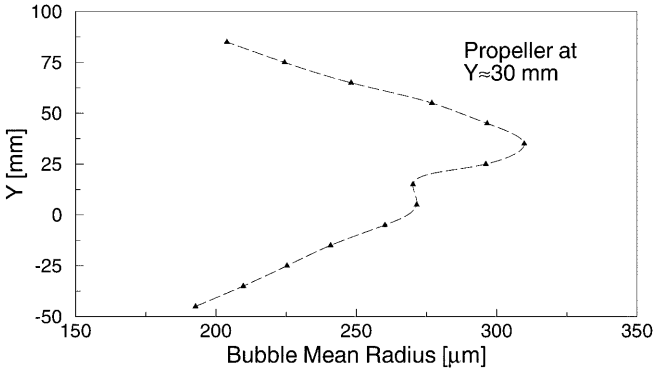


**Fig. 9.** Bubble size: mean radius vs. $Y$

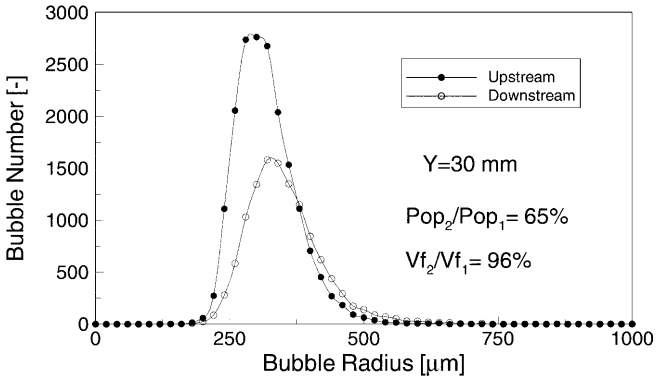


**Fig. 10.** Bubble size: distributions upstream and downstream of the section $Y = 30$ mm

## 7
## Conclusion

A three-dimensional imaging system for the purpose of mapping two-phase bubbly flows has been described and was applied to a vortical flow. On the basis of a defocusing concept that allows simultaneous retrieval of the bubble spatial location and of the bubble size, we designed and fabricated a camera capable of mapping instantaneously a volume of one cubic foot. Velocity measurements showed a mean absolute error corresponding to 0.025 pixel, over the entire range of velocities/displacements explored and over the full interrogation volume. A size procedure was established based on light scattering and demonstrated that the peak intensity of the particle image was a good measure for the particle size. Indeed, the trend found was in excellent agreement with the Mie scattering theory. These conclusions need to be extended through additional and in-depth measurements. Application to a bubbly flow around a propeller provided a remarkable insight into this complex flow. The variations in the mean bubble size were perfectly detected as the bubbles were entrained through the propeller. Finally, the analysis of the bubble size histograms and of the void fractions upstream and downstream of the propeller clearly pointed out that coalescence was the major bubble collective interaction mechanism in this flow.

## References

**Abe M; Yoshida N; Hishida K; Maeda M** (1998) Multilayer PIV technique with high power pulse laser diodes. In: Proceedings of 9th International Symposium on Applications of Laser Techniques to Fluid Mechanics. Instituto Superior Técnico, Lisbon, Portugal

**Barnhart DH; Adrian RJ; Papen GC** (1994) Phase-conjugate holographic system for high-resolution particle image velocimetry. Appl Opt 33: 7159–7170

**Billet ML** (1985) Cavitation nuclei measurements A Review. In: Proceedings of Cavitation and Multiphase Flow Forum. ASME, Albuquerque, N.M., pp 31–38

**Billet ML** (1986) Cavitation nuclei measurements with an optical system. J Fluids Eng 108: 366–372

**Brücker C** (1997) 3D scanning PIV applied to an air flow in a motored engine using digital high-speed video. Meas Sci Technol 8: 1480–1492

**Chen Z; Milner TE; Dave D; Nelson JS** (1997) Optical Doppler tomographic imaging of fluid flow velocity in highly scattering media. Opt Lett 22: 64–66

**Davis GE** (1955) Scattering of light by an air bubble in water. J Opt Soc Am 45: 572–581

**Dean CE; Marston PL** (1991) Critical angle light scattering from bubbles: an asymptotic series approximation. Appl Opt 30: 4764–4776

**Gharib M; Modarress D; Dabiri D; Pereira F; Taugwalder F** (1998) Development and application of a defocusing three dimensional DPIV technique for the mapping of two-phase bubbly flows. In: Proceedings of 9th International Symposium on Applications of Laser Techniques to Fluid Mechanics. Instituto Superior Técnico, Lisbon, Portugal

**Grant I; Fu S; Pan X; Wang X** (1995) The application of an in-line, stereoscopic, PIV system to 3-component velocity measurements. Exp Fluids 19: 214–221

**Griffin OM; Peltzer RD; Reed AM; Beck RF** (1992) Remote sensing of surface ship wakes. Naval Eng J 104: 245–258

**Hofeldt DL; Hanson RK** (1991) Instantaneous imaging of particle size and spatial distribution in two-phase flows. Appl Opt 30: 4936–4948

**Katz J; Gowing S; O'Hern T; Acosta A** (1983) A comparative study between holographic and light-scattering techniques of microbubble detection. In: Proceedings of Symposium on Measuring Techniques in Gas–Liquid Two-Phase Flows. IUTAM, Nancy, France, pp 41–66

**Landa I; Tebay ES** (1970) The measurement and instantaneous display of bubble size distribution, using scattered light. In: Proceedings of 5th Cavitation Forum. ASME, Detroit, Mich

**Mishima K; Hibiki T** (1998) Development of high-frame-rate neutron radiography and quantitative measurement method for multiphase flow research. Nucl Eng Des 184: 183–201

**Naqwi A; Durst F; Kraft G** (1991) Sizing of submicrometer particles using a phase-Doppler system. Appl Opt 30: 4903–4913

**Rockwell D; Magness C; Towfighi J; Akin O; Corcoran T** (1993) High image-density particle image velocimetry using laser scanning techniques. Exp Fluids 14: 181–192

**Stüer H; Maas HG; Virant M; Becker J** (1999) A volumetric 3D measurement tool for velocity field diagnostics in microgravity experiments. Meas Sci Technol 10: 904–913

**Trevorrow MV; Vagle S; Farmer DM** (1994) Acoustical measurements of microbubbles within ship wakes. J Acoust Soc Am 95: 1922–1930

**Van de Hulst HC** (1957) Light scattering by small particles. Wiley, New York

**Willert CE; Gharib M** (1992) Three-dimensional particle imaging with a single camera. Exp Fluids 12: 353–358